J. Earth Syst. Sci. (2019) 128:117
https://doi.org/10.1007/s12040-019-1129-2

Observation of short-term variations in the clay minerals ratio after the 2015 Chile great earthquake ($8.3M_w$) using Landsat 8 OLI data

B Nath[1,2,3,*], Z Niu[1,2] and A K Mitra[4]

[1] *The State Key Laboratory of Remote Sensing Science, Institute of Remote Sensing and Digital Earth (RADI), Chinese Academy of Sciences (CAS) and Beijing Normal University, P.O. Box 9718, Datun Road, Chaoyang District, Beijing 100 101, People's Republic of China.*
[2] *College of Resource and Environment, University of Chinese Academy of Sciences (UCAS), Yuquan Road 19, Shijingshan, Beijing 100 049, People's Republic of China.*
[3] *Department of Geography and Environmental Studies, University of Chittagong, Chittagong 4331, Bangladesh.*
[4] *Department of Earth Sciences, Indian Institute of Engineering Science and Technology, Shibpur, Howrah 711 103, West Bengal, India.*
**Corresponding author. e-mail: nath.gis79@gmail.com*

MS received 13 April 2018; revised 14 September 2018; accepted 15 October 2018; published online 8 May 2019

In this paper, we explore the potential use of available free Landsat sensor data to investigate the short-term variations (STV) in the clay mineral ratio (CMR) following the 2015 Chile great moment magnitude earthquake ($8.3M_w$). The present investigation was carried out in the absence of ground observation data. Landsat 8 Operational Land Imager (OLI)-based multi-temporal imageries of before, after and non-earthquakes were used to derive the above parameter by applying the band ratio approach of bands 6 and 7, where the before and after imageries were compared with non-seismic event images as well as for validation. For the temporal automatic lineament data extraction and final lineament mapping, band 8 (panchromatic) was used by applying the LINE algorithm technique of PCI Geomatica, and ArcGIS 10.5 software, respectively. All these derived products finally interact with the regional geology, fault line and lineament systems. The results reveal that CMR can easily identify the STV at temporal scales before and after the earthquake, while both are normal during non-earthquake time. However, this variation was observed in all three buffer zones (i.e., 50, 100 and 150 km buffer) and highly pronounced especially in the fault adjoining areas. Therefore, we found this research to be effective and could be used as an alternative method for future earthquake studies.

Keywords. Clay minerals ratio; earthquake; Chile; Landsat 8 OLI; multispectral.

1. Introduction

Remote sensing has been used in earthquake research since the 1970s, with the first appearance of satellite images. The Landsat 8 Operational Land Imager (OLI) optical sensor is a powerful one with some advantages over its predecessors and its 16-day revisitation capacity over the same area helps us choose this sensor and investigate the subsequent changes in the clay minerals ratio (CMR)

Supplementary material pertaining to this article is available on the *Journal of Earth System Science* website (http://www.ias.ac.in/Journals/Journal_of_Earth_System_Science).

in earthquake-stricken areas. We all know that our mother Earth is continuously bubbling with tectonic activity because of which there is a huge tectonic force continuously acting on the tectonic plates and the associated rocks, causing the continuous accumulation of stresses within the rock bodies. Then, when the accumulated stresses are too much that the associated rock bodies cannot bear with, they disrupt and release the accumulated energy in the form of earthquakes. These fault zones are avenues for various hydrothermal fluids and could be a potential zone for clay mineral formation (Barton *et al.* 1995). Water is essential for clay mineral formation and most clay minerals are described as hydrous alumino silicates.

Remote sensing applications were vastly used and well established to investigate various aspects of earthquake-related phenomena such as liquefaction (Gupta *et al.* 1998; Mohanty *et al.* 2001; Ray *et al.* 2001; Singh *et al.* 2001), damage (Sharma *et al.* 2003), landslides (Saraf 2000), and co-seismic fault model (Solaro *et al.* 2016), hydrothermal alternation zones and band ratios (Madani *et al.* 2003). Satellite images basically provide a clear synoptic view of the Earth's surface where manifestations of hydrothermal wall rock alterations and gross structural features can be discerned and this typical thought was established by several earth scientists in different time periods (Hoppin *et al.* 1973; Houston 1973; Jensen and Bateman 1981; Sabins 1987; Drury 1993; Zhang *et al.* 2016). Hydrothermal alteration zones in a tropical region such as the Bau gold field area of Sarawak, Malaysia, was investigated with structurally controlled gold mineralisation indicators, including iron oxides and clay minerals, and faults and fractures have been detected using the remote sensing satellite data (Pour *et al.* 2013). Recently, Landsat 8 OLI data have been used for the hydrothermal alteration mapping in the Sarcheshmeh copper mining district of the southeastern Islamic Republic of Iran (Pour and Hashim 2015). Moreover, a comparative study of Landsat 8 OLI and Landsat 7 ETM+ was conducted in mapping the geology and visualising the lineaments of the central regions of Kenya (Mwaniki *et al.* 2015).

Chester and Logan (1986) describe the fault structures and the fault core and mentioned that the fault core is a part of the fault zone, where most of the slip and high shear stress accumulates. Fault zone and weakening mechanisms were also studied with the internal structure (Chester and Logan 1986; Forster *et al.* 1991; Chester *et al.* 1993; Newman and Mitra 1994). The fault zones are commonly associated with the occurrence of clay horizons (Caine *et al.* 1996; Kuo *et al.* 2012; Si *et al.* 2013). Several authors have shown that clay minerals form along fault zones or weak zones (Moore 1989; Barton *et al.* 1995) and play an important role in lowering frictional strengths (Zoback *et al.* 1987; Hickman 1991; Wintsch *et al.* 1995). Clays develop in the fault zones by the infiltration of aqueous phases. Apart from the fault zones, clay horizons may occur in detachment zones in the fold thrust belt (Warr *et al.* 1996; Vrolijk and van der Pluijm 1999). The Earth's crust develops cracks before an earthquake and creates small quakes as precursors, and for this reason, there is a change of pore water pressure and its composition and, subsequently, the volume increases; this behaviour is called 'dilatancy' (Towhata 2008). During an earthquake, rocks get dilated and numerous fractures are developed, and as a result, the rock mass becomes hydrated and clay minerals are formed. As deformation proceeds, the pattern of fractures and lineaments changes, and thereby, the occurrence of clay minerals also changes in the earthquake belt. Besides the above-mentioned studies, fault-related authigenic clay formation was observed in a 2008 Wenchuan earthquake study (Si *et al.* 2013) and clay mineral occurrence study along fault zones by Fitts and Brown (1999).

The Landsat satellite sensor has the capacity to generate fruitful data in the short-wave infrared (SWIR) range. Several researchers have used multispectral remote sensing technology to extract alteration information (Chen *et al.* 2009a, b). Band ratio is a common method to process remote sensing images, and it also enhances the difference by taking the digital number ratio of two bands or several bands, highlighting the features in the original grey scale image (Inzana *et al.* 2003). Thus, CMR is defined as the ratio of band 5 to band 7, which can be used to identify mineral groups such as clays, micas, carbonates, sulphates, and various alteration of minerals. Several other researchers have frequently used the mineral index method to extract information from multi-temporal data sources, i.e., Landsat thematic mapper (TM), enhanced thematic mapper (ETM) and the advanced space-borne thermal emission and reflection radiometer (ASTER) data (Gad and Kusky 2007; Khan and Mahmood 2008; Massironi *et al.* 2008). Meanwhile, Sabins (1999) studied and extracted clay and alunite information using the ratio image of TM5/TM7 of Landsat data.

The study area is located in the Illapel regions of Chile, a coastal area which is one of the most earthquake prone regions in the world. The area already experienced numerous earthquakes with different magnitudes from light to great categories along with volcanic eruptions. The historical records since 1973 showed that Chile has had more than a dozen earthquakes of magnitudes 7.0 and above (CNN 2015) and have a great impact in the areas such as land and coastal areas. However, no research work has been done on seismic studies by utilising the remote sensing and GIS integrated approach considering Landsat 8 OLI data of any magnitudes of earthquakes in general and short-term variations (STV) of CMR in particular. The geological mapping of this particular region is found at the regional level (USGS data catalog: http://certmapper.cr.usgs.gov). Lineaments were extracted relying on temporal Landsat 8 OLI panchromatic (PAN) band 8, allowing the identification of new geological and structural elements. Therefore, lineaments are seen as 'rectilinear or slightly curvilinear' features that are the reflection of the geological phenomena occurring on the Earth's surface (Hung *et al.* 2005) and several other techniques involving remote sensing were also applied to detect lineament (Al Rawashdeh *et al.* 2006). Until date, the study of earthquakes incorporates various techniques or methodologies such as GPS data, geomorphology, fault and thrust analysis, lineament pattern analysis, etc., but no one have correlated the mode of occurrence of clay minerals with earthquake-prone zones including regional geology, fault and temporal lineaments data derived from the same data source i.e., Landsat 8 OLI data, although the occurrence of clay minerals or clay horizons has been thoroughly studied along structurally weak zones such as fault zones, thrust zones, shear zones, etc. The integration of remote sensing derived data in relation to other information possibly suitable for clay minerals features identification, alteration of minerals, abundance of AL–OH (such as those clay and sulphate minerals) and CO_3 minerals in the present study.

In addition, CMR extracted with the band ratio approach from ENVI (environment for visualising images) software version 5.3 was used. The period covered for this study refers to the southern spring. The study has been performed under three-different scenarios, i.e., before earthquake (BEQ), after earthquake (AEQ) and non-earthquake (NEQ), where an epicentre-based buffer drawn within 50 km (0–50 km distance), 100 km (50–100 km distance) and 150 km (100–150 km distance), respectively, and data were extracted, analysed and documented based on multi-temporal datasets. The first two scenarios such as BEQ and AEQ have been used for comparison and validation with two NEQ datasets. Moreover, these earthquake prone areas were particularly rich in mineral resources. The variation in the values of the CMR from these areas is a solution to the problem of earthquake study. Therefore, the aim of the current study is to understand the STV of the CMR in the great magnitude earthquake affected ($8.3M_w$) Illapel regions of Chile using Landsat 8 OLI data in relationship with the geological structures which is a unique approach in this field. In this context, we use the term CMR which is a normalised value of the relative appearance of the clay mineral content in a particular zone of interest.

The direct objectives of the present study are to (i) use freely available multi-temporal Landsat 8 OLI imageries for CMR data extraction at temporal scales in the great Illapel region of the Chile earthquake, 2015; (ii) identify the spatio-temporal variations of CMR at three buffer zones coupling with the geological structures, i.e., regional geology, fault lines and temporal lineaments data; (iii) analyse CMR variations considering the integrated geological data based on the pixel values derived from the arbitral transect drawing at temporal scales; and (iv) determine the areas of CMR variations considering the statistical data, their relationship and significance.

2. Data and study area

2.1 *Datasets*

For the present investigation datasets utilised included Landsat 8 OLI sensor Images, acquisition from USGS Landsat standard level-1 products archive (USGS 2015: http://earthexplorer.usgs.gov) with a spatial resolution of 30 m. The following path/row, i.e., 1/82 with bands 6 and 7 was considered for the present investigation. In this study, six multi-temporal satellite scenes of the same area (epicentre-based tile image) from 12 August 2014 to 2 October 2015 were considered, and three of them were used for BEQ, one for AEQ and the other two were used for NEQ change evaluation. The detailed datasets considered for the study are given in table 1.

Table 1. *Details of datasets used in the present study.*

Sl. no.	Satellite sensor	Date of image acquisition	Scenario	Path/row	Band used	Resolution (m)
Illapel of Chile: category: great: earthquake date: 16 September 2015						
1	Landsat 8 OLI	30 July 2015	BEQ	1/82	6, 7 and 8	30 and 15
2	Landsat 8 OLI	15 August 2015	BEQ	1/82	6, 7 and 8	30 and 15
3	Landsat 8 OLI	31 August 2015	BEQ	1/82	6, 7 and 8	30 and 15
4	Landsat 8 OLI	2 October 2015	AEQ	1/82	6, 7 and 8	30 and 15
5	Landsat 8 OLI	14 July 2015	NEQ	1/82	6, 7 and 8	30 and 15
6	Landsat 8 OLI	12 August 2014	NEQ	1/82	6, 7 and 8	30 and 15

Source: USGS-Earth explorer Landsat 8 Archive. In column six, band 6, 7, and 8 refers short-wave infrared 1 (SWIR 1), short-wave infrared 2 (SWIR 2) and Panchromatic band (PAN), respectively.

However, for the present case, the epicentre and geo-location information were retrieved from recent earthquake databases of the USGS earthquake hazard program site (USGS 2015), which was verified with Google earth and later plotted as the epicentre point highlight with a red asterisk. In addition, a country level polygon shapefile and a geological fault line were incorporated into the analysis which were downloaded from the Geotech-Geotechcenter.org under Map Library and Data Resources (http://www.gadm.org/country) and GitHub-cossatot/gem-global-active-faults, respectively, and the geological layer GIS data shapefile of the South America Geologic Map (geo6ag) was available from the USGS Geologic Map-Catalog Data Gov (USGS data catalog – South America Geologic Map (geo6ag), https://catalog.data.gov/dataset). In the next step, to provide a more intuitive look at the image data, a PAN band (band 8, resolution 15 m) of all six Landsat 8 OLI scenes considered in this study were used for lineament map preparation by applying standard sets of parameters.

2.2 *Study area*

For the present research, we have selected our study site in the earthquake prone area i.e., the Illapel regions of Chile, where weather, local topography, geomorphology, geomagnetic anomaly and tectonic stress field may have an influence and are varied. The Illapel earthquake of Chile struck on 16 September 2015 at 22.54 UTC in the Pacific Ocean, in the sea area west of Central Chile, offshore of Illapel, with an $8.3M_w$ at a depth of 25 km (USGS 2015).

This great category earthquake reported along the interface between the subduction of Nazca overriding the South American plates. The geographical extent of the Illapel and adjoining areas is in the region of 30°41′17.95″S–32°47′47.90″S latitude and 70°05′23.03″W–72°36′34.63″W longitude. The epicentre was located (geographical position: 31°34′12″S and 71°39′14.04″W) approximately midway between the port cities of Valparaiso and Coquimbo, 250 km NW of Santiago. The location of the study area and geological information are shown in figure 1.

The geological shapefile was subset based on the study area boundary and the available acronyms in the database were further illustrated with a proper naming convention. The study area consists mainly of nine sub-areas which are the accident potential zone (APZ), cretaceous palaeozoic (CP)-sedimentary rocks, cretaceous volcanics (Cv), Jurassic (J)-sedimentary rocks, Karst (K)-sedimentary rocks of the palaeozoic age, mesozoic–cenozoic intrusives (MCi)-igneous and metamorphic rocks, quaternary (Q)-sedimentary rocks, tertiary (T)-sedimentary rocks and triassic (Tr)-sedimentary rocks, respectively (figure 1b). The major parts of the study area are composed of MCi shares in the north-western, central and parts of the eastern belt which is reflected with medium to very high CMR pixel values represented as clay minerals. The north-western and small parts are composed of APZ close to the Pacific coast line. In the western parts below the marked epicentre, sedimentary rocks of the Tr age present indicate clay minerals with high to very high CMR pixel values. Moreover, the northern part and central-southern direction with the N–S aligned further, flanked by the south-eastern parts, and a tiny part in the southern extent is composed of K which is a result of the dissolution of a layer of soluble bedrock, usually carbonate rock such as

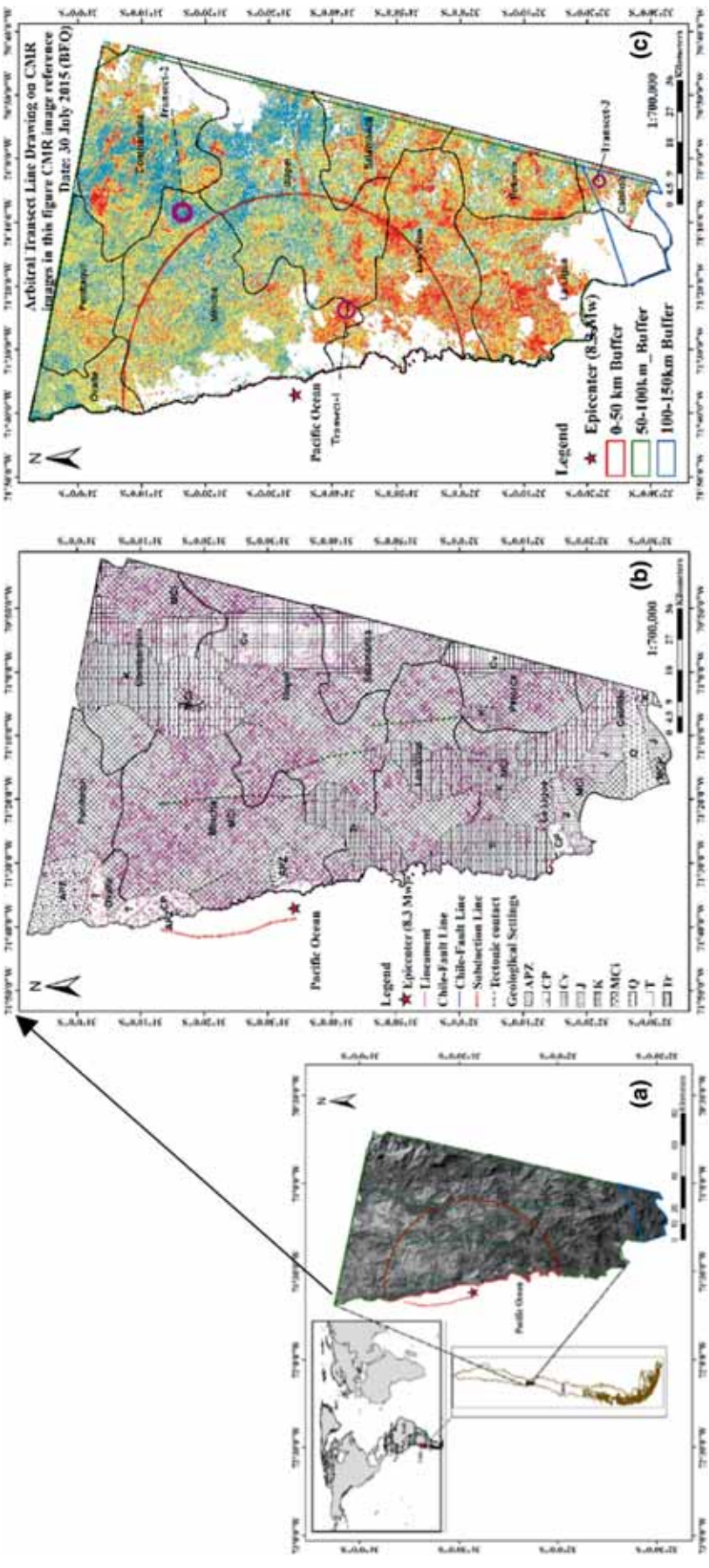

Figure 1. Location of the study area, its geological map and arbitral transect profile location: (**a**) the inset map pointing to Chile areas highlighted with a red asterisk showing parts of the global map; and a closer view of the Chile country boundary, the small bounding area represents the study location and on the right, the larger view of the study area (Illapel regions of Chile) represents the radiometric corrected image shown in black and white rendered mood for display only; (**b**) the simplified geology of the study area at the regional level with an overlay of the lineament data (extracted from band 8 of Landsat 8 OLI) and fault lines (modified from South America Geologic Map-geo6ag-USGS Data Catalog); (**c**) three arbitral transect profiles location selected in three buffer zones for CMR variations study, where transects are bounded with circles and marked as Transect-1, Transect-2, and Transect-3, respectively.

limestone or dolomite. The north-eastern parts are composed of Cv, and in the southern part below the MCi, and J, Q dissects the region in the W–E direction with no significant fault line presence over there. The lineament data derived from the Landsat 8 OLI data (displaying as an example of 30 July 2015) using PAN-band 8 was observed at a high to very high lineament concentration in the MCi formation area over the study regions (i.e., Mincha, Illapel, northern part of Salamanca, parts of Los Vilos and Petorca) (figure 1b). In the light of the structural point of view, this study area is characterised by major and minor fault lines within the land territory and the subduction line in the coastal offshore area. However, there is no previous research available in this study region based on this parameter (i.e., CMR), thus it helps us to consider a way forward to know the STV of this parameter in the great magnitude earthquake of the Illapel region, Chile.

3. Methodology

Cloud-free Landsat imageries are always have an advantage over cloud-present images. As we are presently dealing with the recent past great magnitude 8.3 (M_w) earthquake study of the CMR, the presence of clouds over images was identified as a problem, which may have lost many vital information of the ground surface. Due to the presence of the clouds on the BEQ and AEQ images, it was impossible to extract data from the entire satellite scene. Thus, before we proceed to data extraction, we have used auto Fmask algorithm-3.2.1 beta version to calculate the images free from clouds, cloud shadow, water features, snow, etc. which performed masking for each original image automatically in the MATLAB 14b software platform. The default threshold value obtained from the algorithm was applied for the operation. On the other hand, two other images of NEQ were not considered for the cloud masking operation due to the presence of 0.72% cloud coverage in 14 July 2015, and 0.92% cloud coverage in 12 August 2014 images, respectively (USGS earth explorer metadata file of respective Landsat 8 OLI images). The aim of this study was to use clear land pixel images without any interference of cloud, cloud shadow, snow (if it contained by image) and water areas, to exactly represent the variations of this parameter (i.e., CMR). For the present investigation, two bands of SWIR of multispectral bands are used for data extraction and for further analysis.

In this paper, we have generated CMR maps derived from the Landsat 8 OLI satellite data by considering the band ratio approach of two SWIR bands (SWIR 1: band 6 and SWIR 2: band 7, respectively). After preprocessing of images using the ENVI 5.3 software, radiance corrected images were imported in the ArcGIS 10.5 environment for image analysis. The 3D spatial analyst tools of the ArcGIS 10.5 software used to generate maps based on temporal datasets, where the division function under a math operator of spatial analyst tool was used for data extraction. For the study of spatio-temporal variations of this earthquake, we have considered six images, with three scenes for BEQ, one for AEQ and the other two for NEQ investigations. Furthermore, an epicentre-based buffer zone (50, 100 and 150 km) was created and plotted in the ArcGIS software (version 10.5) and performed the masked operation for all considered GIS layers based on the buffer boundary (i.e., 0–50 km distance, 50–100 km distance and 100–150 km distance) to closely examine its spatial extent as well as the spatio-temporal data variations. The CMR data variations were further interpreted with regional geology, lineaments and fault lines associated with this parameter, as well as NEQ time datasets finally considered for data validation with the BEQ and AEQ data.

However, for better interpretation, three arbitral transect profile curves were drawn in three buffer zones to represent the CMR alteration of the study area. Therefore, based on the temporal classified images (i.e., very low to very high category CMR pixel values were taken as reference to represent data variability) within each transect line. All temporal CMR profile variations were closely examined and marked with a change alternation signature compared with the minerals spectra available from USGS spectral library viewer using ENVI (5.3 version) software. The overall workflow of the present research is highlighted in figure 2 and the details of the methodological breakdown are highlighted in sections 3.1–3.4.

3.1 *Pre-processing of Landsat imageries*

In this pre-processing stage, our prime focus is on using only clear land images for data extraction. These clear land images of the study area were further used for radiance value estimation by radiometrically calibrated and converted DN values to

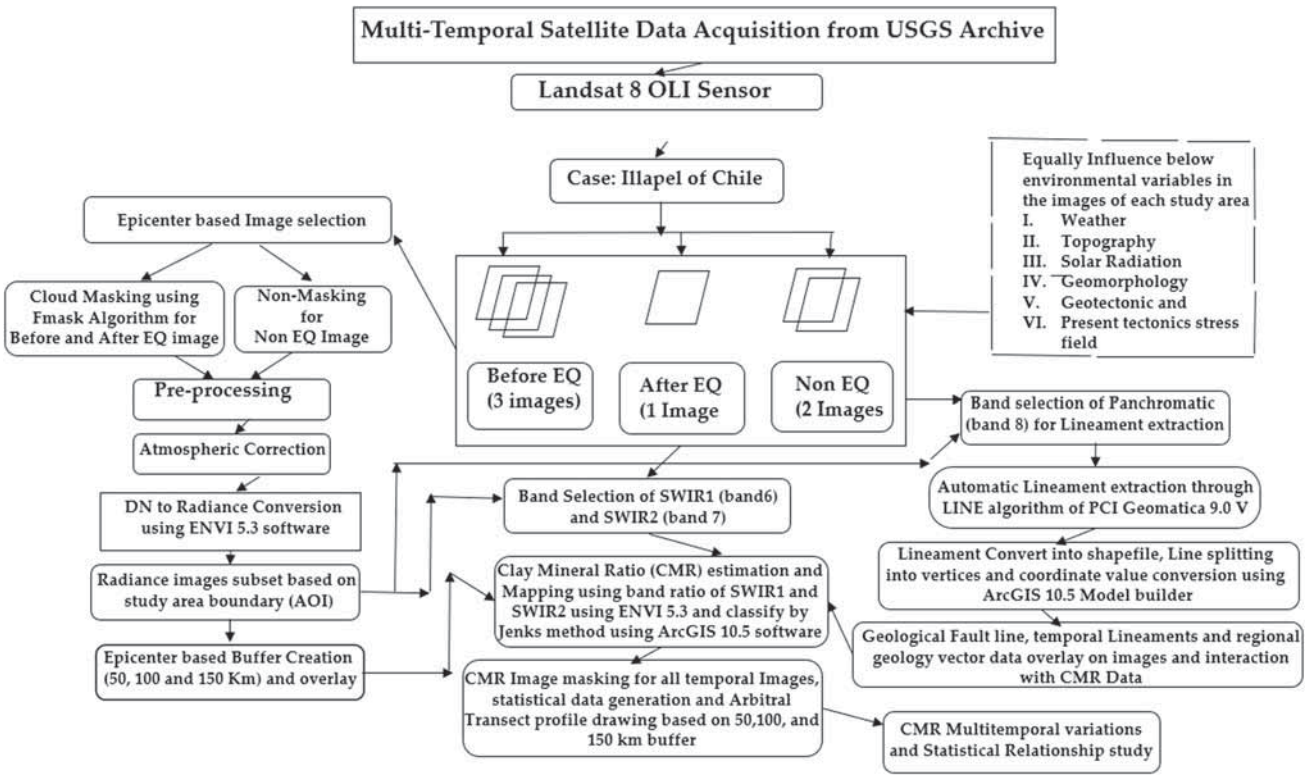

Figure 2. Flow chart of the methodology used in this research.

radiance corrected images as an output of a band interleaved by line (BIL). For this conversion, data type was considered as float and FLAASH settings with a default scale factor 0.1 were used for the radiometric correction of each scene performed by the ENVI software (version 5.3). Landsat 8 OLI satellite sensor-based temporal imageries with a 30-m spatial resolution of the SWIR bands 6, 7 and 15-m resolution PAN (band 8) were considered for the present analyses. Furthermore, for processing and extraction of lineaments, PAN was considered by the set standard algorithm parameters provided by the PCI Geomatica 9.0 version software. Finally, all derived images were subset based on an area of interest of this case study and the datum and projection parameter used was WGS 1984 UTM Zone 19 S, and the metre was considered a linear unit.

3.2 *CMR mapping, spatio-temporal variations and uncertainty of average estimation*

In this section, we tried to generate CMR images by considering radiance corrected images of the study area using the band ratio approach available from the toolbox function of the ENVI 5.3 software, where we considered only the SWIR 1 and SWIR 2 bands from all available Landsat 8 OLI bands. Generally, this band ratio highlights hydrothermally altered rocks which contain clay, and alunite is designated with the following formula proposed by Drury (1987) as shown in the following equation:

$$\mathrm{CMR} = \frac{\mathrm{SWIR\ 1}}{\mathrm{SWIR\ 2}}, \tag{1}$$

where the shortwave-infrared: band 6-SWIR 1 range is 1.57–1.65 μm and band 7-SWIR 2 range is 2.11–2.29 m for Landsat 8 OLI, respectively. However, this band ratio can also indicate carbonate mineralisation.

For this research, the results highlighted in the grey scale image as the band ratio output in ENVI, further imported as a.tiff file classified in the ArcGIS 10.5 software by applying the natural breaks (Jenks) classification method with five class output ranges rounded with two decimal and categorised as very low, low, medium, high and very high category, based on the CMR ratio of each image. This index works well with any multispectral sensor with bands that fall within

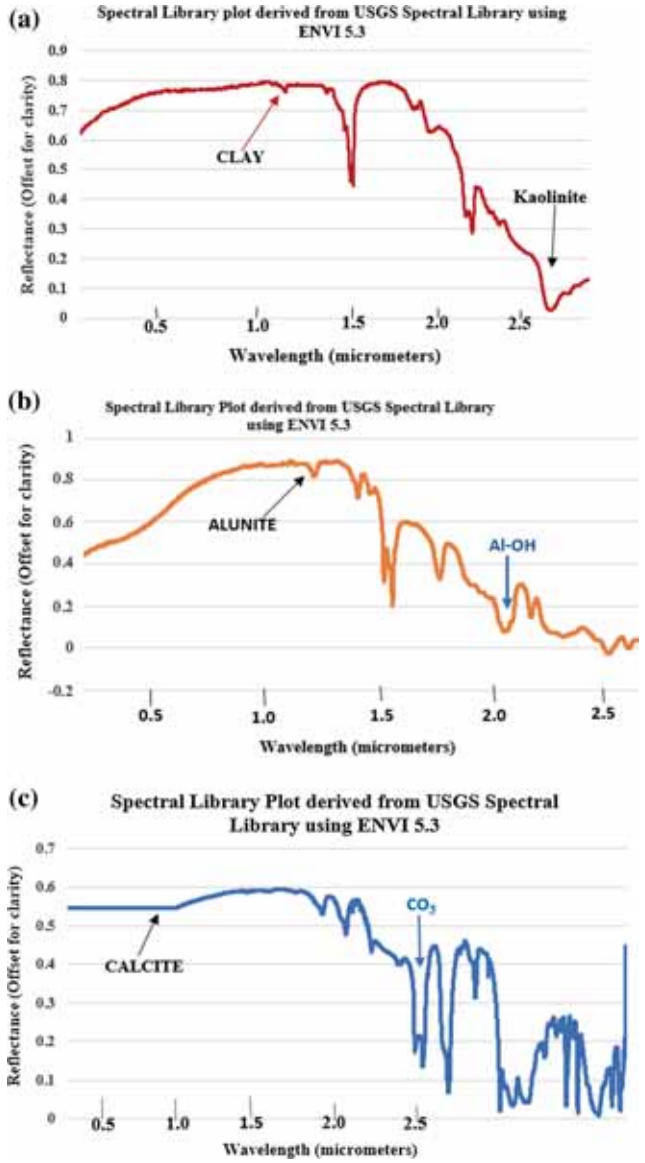

Figure 3. Laboratory spectra of clay, alunite and calcite derived from USGS spectral viewer of ENVI 5.3 software: (**a**) clay spectra profile represents Kaolinite considering input spectra of Kaolinite-CM3 [W1R1Ba AREF], (**b**) alunite spectra profile represents Al–OH considering input spectra of alunite HS295.3B [W9R4Naaa RREF] and (**c**) calcite spectra profile representing CO_3 minerals considering the input spectra of Calcite-WS272 [W9R4Naaa RREF].

the listed ranges (Geology Indices Background, https://www.harisgeospatial.com/docx). For Landsat TM and ETM+, this corresponds to band 5 (SWIR 1) and band 7 (SWIR 2), whereas, in the Landsat 8 OLI image, it corresponds to band 6 (SWIR 1) and band 7 (SWIR 2), respectively. This research only deals with the Landsat 8 OLI sensor. For this study, two-short wave infra-red bands were considered for generating CMR images. In the next stage, CMR arbitral profile has been extracted on three transect lines based on temporal data, marked and compared with the mineral spectral reflectance curves (i.e., clay, alunite and calcite) (figure 3) available in the USGS spectral library viewer from the ENVI 5.3 software. Finally, our focus is only to identify the spatio-temporal variations of the CMR changes in the great category earthquake of the Illapel regions, Chile, at the three-buffer levels which are masked and distributed in the following manner, i.e., 0–50, 50–100 and 100–150 km distance.

However, there is no literature available on the uncertainty or error in this proposed CMR index (Drury 1987) only to represent that the band ratio approach works well with any multispectral data which fall within the reflectance range of SWIR 1 and SWIR 2. In this study, we have calculated the uncertainty of average in the mean values, based on the temporal data extracted CMR pixel values for these three buffer zones with the following formula as shown in equation (4), to know the accuracy of the CMR index derived results. This formula is the final output for calculating the uncertainty of average by considering the two equations as shown in equations (2 and 3), respectively:

$$\text{Average mean} = \frac{\text{Sum}}{\text{number count}}, \tag{2}$$

$$\text{Uncertainty} = \frac{\max - \min}{2}, \tag{3}$$

$$\text{Uncertainty of average} = \text{Average mean} \pm \text{uncertainty}. \tag{4}$$

3.3 *Lineament mapping and analysis*

Structures appear as either linear features for faults or curvilinear for underlying domes in an image (Drury 1987; Lillesand *et al.* 2015). Lineament extraction and mapping for the regional scale has been performed based on the same source (i.e., Landsat 8 OLI) using the PAN band (band 8) applied along with CMR data. The same temporal datasets were used to know the structural variation with the CMR datasets. For the lineament data extraction and mapping, the corresponding default values of the LINE algorithm of PCI Geomatica 9.0v were used such as RADI-radius of the filter in pixels (10), GTHR-threshold for the edge gradient (50), LTHR-threshold for the curve length in pixels (30), FTHR-threshold for the line fitting error in pixels (3), ATHR-threshold

for the angular difference in degrees (30) and DTHR-threshold for the linking distance in pixels (20). For line split generation ArcGIS 10.5 model builder was used to automate GIS processes by linking data input, tools/functions and data output, saved into the shapefile format. This feature extracted as a compound line, split into a single line at the vertices, recorded the polylines in a vector layer which was further used for the overlay operation to match with the regional fault lines, and plotted as an overlay with 55% transparent adjacency applied on it to provide a more intuitive look of the temporal CMR images. The total number of lineaments and their length (in kilometres) were measured using the ArcGIS 10.5 software on a temporal basis, which is considered a better interpretation of the CMR variations study.

3.4 *Statistical analysis*

In the final evaluation process, we have statistically analysed the temporal data variations in two ways: (i) variation study through the bar diagram displayed with an error bar with a trend line according to three different buffer extents, where the mean value distribution was presented against the observed date and (ii) the individual buffer-based temporal relationship of mean CMR was observed with the coefficient of variations (CV), representing the coefficient of determination (i.e., R^2) from linear regression analysis. However, the data conversion of CMR to the coefficient of variations (CV) was performed to know the spatial variations of the datasets and expressed with the following formula as shown in

$$\mathrm{CV} = \frac{\sigma}{\mu} * 100\%, \tag{5}$$

where $\mathrm{CMR}_{\mathrm{mean}}$ is the mean clay mineral ratio (designated as μ) and σ is the standard deviation of this parameter. The relative variability was measured by the coefficient of variations, which can help identify a certain value as anomalous. The corresponding figures and tables were generated using Microsoft Excel 2016. Moreover, this statistical analysis helps us target the anomaly date along with identifying the buffer zone of the highest variations which can be used for the study of this great magnitude earthquake variations.

4. Results and discussion

The detailed assessment and results obtained using the band ratio approach in this study derived from the analysis of radiance corrected multi-temporal Landsat imageries are described in the following sections. While considering this sensor, the images were subset based on the study area of interest. All CMR maps for the Illapel areas were estimated based on equation (1) of the methodology discussed in section 3.2, and the masking of the buffer of those images performed was based on the method discussed in section 3 (methodology), respectively. The extracted lineament data were used as an overlay on each corresponding CMR image with transparent adjacency, along with a regional geological map and faults lines were incorporated for better interpretation, to show the detection of the CMR variations and its changing phenomena with the geological settings as well as in the lineament changes during this time period.

4.1 *Spatial patterns and temporal variations of CMR in relationship with lineaments (based on the overall scenario)*

The overall scenario-based spatio-temporal distribution of CMR in relationship with the extracted lineaments data in the Illapel region, Chile, from 12 August 2014 to 2 October 2015 is shown ‘in figure 4(a–f). As the study progressed, we focused on a buffer-based analysis to closely examine the CMR variations under three different scenarios in relationship with the lineament data and other ancillary information which is shown in section 4.2. In this study, for overall CMR distribution, the corresponding maps were prepared on a 1:750,000 scale (area covered: $10,884.60\,\mathrm{km}^2$) by applying the natural breaks (Jenks) classification method followed by five classes (see section 3). Due to space limitation, the overall descriptive statistical results of temporal lineaments data are only quoted in the text and not presented here, but they are available as a supplementary data file (see supplementary table S1).

The CMR values observed mostly in the range of 0.35–1.68 across the image on 30 July 2015 and the number of lineaments was observed as 25,910 with minimum, maximum and mean length calculated to be 0.45, 5.42, and 1.0 km and the SD value observed was 0.55 (48 days BEQ strike) (figure 4a). The CMR minimum, maximum and

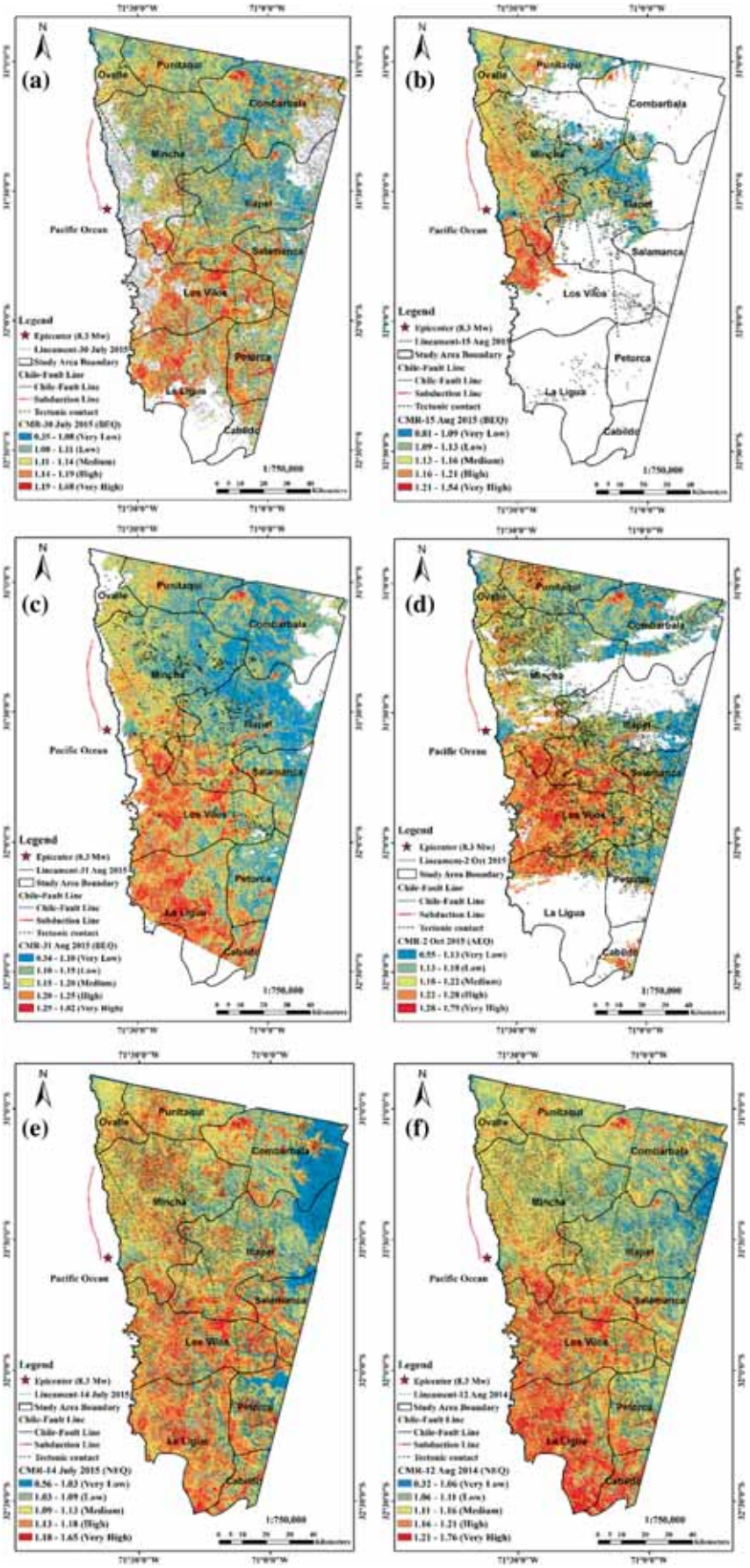
(a)
(b)
(c)
(d)
(e)
(f)
Punitaqui
Ovalle
Combarbala
Monte Patria
Illapel
Salamanca
Los Vilos
Petorca
La Ligua
Cabildo
Pacific Ocean
Legend
1:750,000

mean values were observed as 0.35, 1.68 and 1.12, respectively, in this stage (calculation was performed using ArcGIS 10.5 software). The epicentre is located in the Pacific Ocean which is an off-shore area near the Chilean coastline boundary (indicated by a red asterisk). The CMR value was increased and this change was first noticed on 15 August 2015 (32 days before the earthquake) and lineaments are 5.61 times lower (number of lineaments observed was 4619) than the initial stage which is a clear sign of structural disturbance as observed through the lineament changes in the study area. The major problem on that particular day was the clouds which obstruct visualisation of the details, thus, a smaller number of lineaments appeared in the image (figure 4b), and minimum, maximum, mean and SD values were observed at 0.03, 1.46, 0.33 and 0.18 km, respectively. During earthquake, rocks get dilated and numerous fractures develop as a result, rock masses become hydrated and clay minerals are formed. As deformation proceeds, patterns of fractures and lineament changes occurred, so the occurrence of clay minerals also changed in the earthquake belt.

However, on 31 August 2015 (16 days before the earthquake), based on the entire scene, the CMR ratio values were increased along the south-western part of the Chilean coast and surrounding the epicentre area. The values were comparatively increased in the southern part of Mincha, south-western part of Illapel, north and north-western part of Los Vilos and the south-western part of La Ligua. Thus, this clearly indicates the CMR changes had occurred BEQ (figure 4c). Similarly, lineament changes still continue with further deviation, while the number of lineaments appeared to be 2830, and the maximum and minimum lengths were found to be 3.62 and 0.87 km, respectively. The data suggest that before 16–32 days of the main earthquake event, the surface and underlain geological structures both passed critical time through gaining strains, energy from the rock surfaces and hydrothermal alterations created by the geologically active rocks of this area. The concentration of clay minerals and their corresponding ratio values largely increased after the earthquake stage too with the increasing number of lineaments (15,903), and the maximum and mean length were observed to be 4.36 and 0.97 km, respectively (figure 4d) as the Earth's surface was trying to retain its original status. On the other hand, CMR values also observed a normal range in both NEQ images along with the number of lineaments and length observed being similar to those on 30 July 2015 (figure 4e and f).

Figure 4. CMR distribution over the Illapel earthquake regions. Parts (**a**–**d**) represent the spatio-temporal variation of the CMR of the Illapel areas BEQ and AEQ: (**a**) 30 July 2015 (48 days before); (**b**) 15 August 2015 (32 days before); (**c**) 31 August 2015 (16 days before); (16 September 2015, 8.3M_w earthquake occurred) and (**d**) 2 October 2015 (16 days later) scenario of AEQ data. White area in image represents cloud, cloud shadow and water masked pixels (not considered for the study); and (**e** and **f**) represent CMR in the same areas in the NEQ time: (**e**) 14 July 2015 and (**f**) 12 August 2014, respectively. All figures present CMR distribution along with displaying extracted lineament data and regional fault lines.

4.2 *Spatio-temporal variations of CMR with lineament changes based on three buffer zones*

All temporal buffer masked images are classified in the five-class range and were developed for data comparison at temporal scales, which help to better understand the changing pattern of the CMR ratio under three different scenarios (i.e., BEQ, AEQ and NEQ). These three buffer zones (i.e., 50, 100 and 150 km) measured from the proportion of the total area were 3531.47, 6951.42 and 401.71 km^2, respectively, and displayed with the red, green and blue colour lines in the image. In this stage, the lineaments were masked out from original extracted lineament data based on three different buffer boundaries using the spatial analyst toolbox of ArcGIS 10.5 software. As mentioned in section 4.1, the geological structure (i.e., lineaments) and available regional fault lines were overlaid on each buffer-based CMR images considered for further interpretation. It is worth mentioning here that, within each buffer zone clouds, the cloud shadow, water and snow in the image areas (see white areas in each image) were masked out at the initial stage of image pre-processing.

The descriptive statistical results (i.e., minimum, maximum, mean, standard deviation and coefficient of variations) of CMR were calculated and are shown in table 2. Meanwhile, our analysis results from this section revealed that data variations were obvious in the BEQ strike and existed only during a certain time period, while they were found to be normal during the NEQ time. In this section, observations of temporal

Table 2. *Spatial distribution and variations of CMR in Illapel (Chile) regions (based on 50, 100 and 150 km buffer) under three different scenarios.*

Sl. no.	Satellite sensors	Image date	Scenario	Min	Max	Mean	SD	CV (%)
Illapel of Chile earthquake: $M_w = 8.3$								
0–50 km buffer distance								
1	Landsat 8 OLI	30 Jul 2015	BEQ	0.70	1.41	1.12	0.04	3.56
2	Landsat 8 OLI	15 Aug 2015	BEQ	0.81	1.44	**1.14**	0.05	**4.39**
3	Landsat 8 OLI	31 Aug 2015	BEQ	0.34	1.47	**1.17**	0.05	**4.27**
4	Landsat 8 OLI	2 Oct 2015	AEQ	0.69	1.60	**1.21**	0.05	**4.13**
5	Landsat 8 OLI	14 July 2015	NEQ	0.61	1.48	1.11	0.04	3.60
6	Landsat 8 OLI	12 Aug 2014	NEQ	0.61	1.52	1.14	0.05	4.39
50–100 km buffer distance								
1	Landsat 8 OLI	30 Jul 2015	BEQ	0.35	1.68	1.12	0.04	3.57
2	Landsat 8 OLI	15 Aug 2015	BEQ	0.86	1.54	**1.12**	0.04	**3.57**
3	Landsat 8 OLI	31 Aug 2015	BEQ	0.65	1.82	**1.15**	0.06	**5.22**
4	Landsat 8 OLI	2 Oct 2015	AEQ	0.55	1.78	**1.18**	0.06	5.08
5	Landsat 8 OLI	14 July 2015	NEQ	0.62	1.66	1.10	0.06	5.45
6	Landsat 8 OLI	12 Aug 2014	NEQ	0.34	1.76	1.12	0.06	5.36
100–150 km buffer distance								
1	Landsat 8 OLI	30 Jul 2015	BEQ	0.98	1.37	**1.13**	0.04	**3.54**
2	Landsat 8 OLI	15 Aug 2015	BEQ	–	–	–	–	–
3	Landsat 8 OLI	31 Aug 2015	BEQ	0.67	1.46	**1.19**	0.06	**5.04**
4	Landsat 8 OLI	2 Oct 2015	AEQ	1.01	1.45	**1.23**	0.06	**4.88**
5	Landsat 8 OLI	14 July 2015	NEQ	0.69	1.38	1.12	0.05	4.46
6	Landsat 8 OLI	12 Aug 2014	NEQ	0.34	1.47	1.19	0.07	5.88

Source: Data extracted using Raster calculator of ArcGIS 10.5 software. The date the earthquake occurred in this case is 16 September 2015. Bold values represent data variations in BEQ and AEQ representing CMR anomalies exist in BEQ compared to the normal stage, but the mean variations continue to increase even after the earthquake and observed maximum in the 100–150 km buffer distance compare to the 0–50 and 50–100 km buffer zones.

variations of CMR based on three buffer masked images are shown in figure 5(a–r). Buffer masked CMR maps were prepared in the same layout size, thus the mapping scales may vary. Therefore, 50 km buffer zone images have been prepared on a 1:400,000 scale to closely observe the CMR variations because of the earthquake epicentre location, whereas 100 and 150 km buffer zone images are prepared on a scale of 1:700,000 due to its longest distance from the epicentre.

In a 50-km buffer zone (0–50 km distance), three major tectonic contact lines were identified where the central one runs in the NS direction further deviated towards the NE to the SW direction. Another fault line crossed over it from the NE to the SW direction, one just downward from it runs directed from the NW to the SE, and another tectonic contact line runs from the NW to the SE direction (e.g., see figure 5a). A small fault line also runs in the W–E direction right from the epicentre. Furthermore, to identify the CMR variations at the buffer level, the five classes category was prepared as shown in figure 4, represented by colour legends from light blue to dark red by applying natural breaks (Jenks) classification of ArcGIS 10.5 software, representing the lowest and highest values of all images. Individual images were labelled as very low to very high category considering their derived ratio values which help observe the CMR changes in a temporal dimension (figure 5a–r). This can help us to observe the CMR increasing phenomena and pixel ratio alteration in time domain. Among these three buffer zones, the lowest minimum and the highest maximum CMR values were observed to be 0.32 and 1.82, respectively. However, the mean CMR was finally considered for further evaluation and the observed variations in the great moment magnitude earthquake are shown in table 2.

In the 100 km buffer zone (50–100 km distance), three tectonic contact lines have presence, where two parallel lines run from the N–S and NE–SW direction, while another one joins vertically crossed over it. The extracted lineament data overlay in this zone grossly followed the

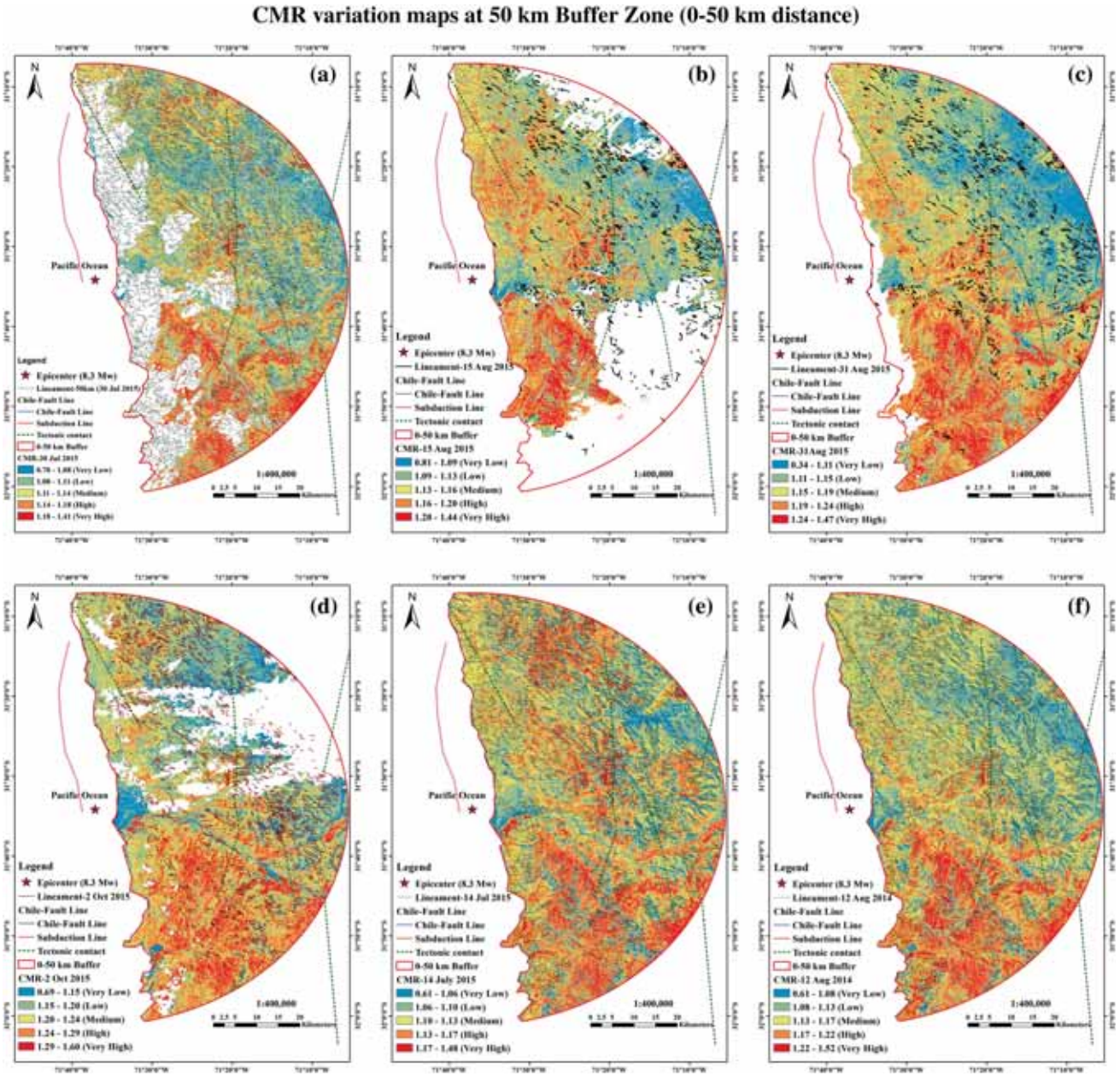

Figure 5. Observations of the clay minerals ratio changes in three different buffer zones (50, 100 and 150 km) under three different scenarios i.e., BEQ, AEQ and NEQ: the same temporal data were used for the variations study in which (**a**–**f**) represent 50 km buffer (0–50 km distance) variations: (**a**) 30 July 2015 (BEQ), (**b**) 15 August 2015 (BEQ), (**c**) 31 August 2015 (BEQ), (**d**) 2 October 2015 (AEQ), (**e**) 14 July 2015 (NEQ) and (**f**) 12 August 2014 (NEQ); (**g**–**l**) represent 100 km buffer (50–100 km distance) variations based on the temporal data and (**m**–**r**) represent 150 km buffer (100–150 km distance) variations based on temporal data. These 100 and 150 km buffer zones time frame are similar as (**a**–**f**).

above trends. These data suggest that outside the 100 km buffer zone (50–100 km distance) was also observed CMR increasing phenomena similar to the 50 km buffer zone. However, the variations were comparatively higher in the 0–50 km buffer zone than the 50–100 km buffer zone observed in the BEQ strike. Eventually, the earthquake struck 16 days later on 16 September 2015. This increasing trend observed AEQ with higher CMR values, i.e., 1.21, 1.18 and 1.23 (50, 100 and 150 km buffer zones), respectively, indicate medium and very high CMR change category (figure 5d, j and p) in the geological structural regions of MCi and Tr (see figure 1b). In order to arrive at a meaningful interpretation, CMR variations of BEQ and AEQ were further compared

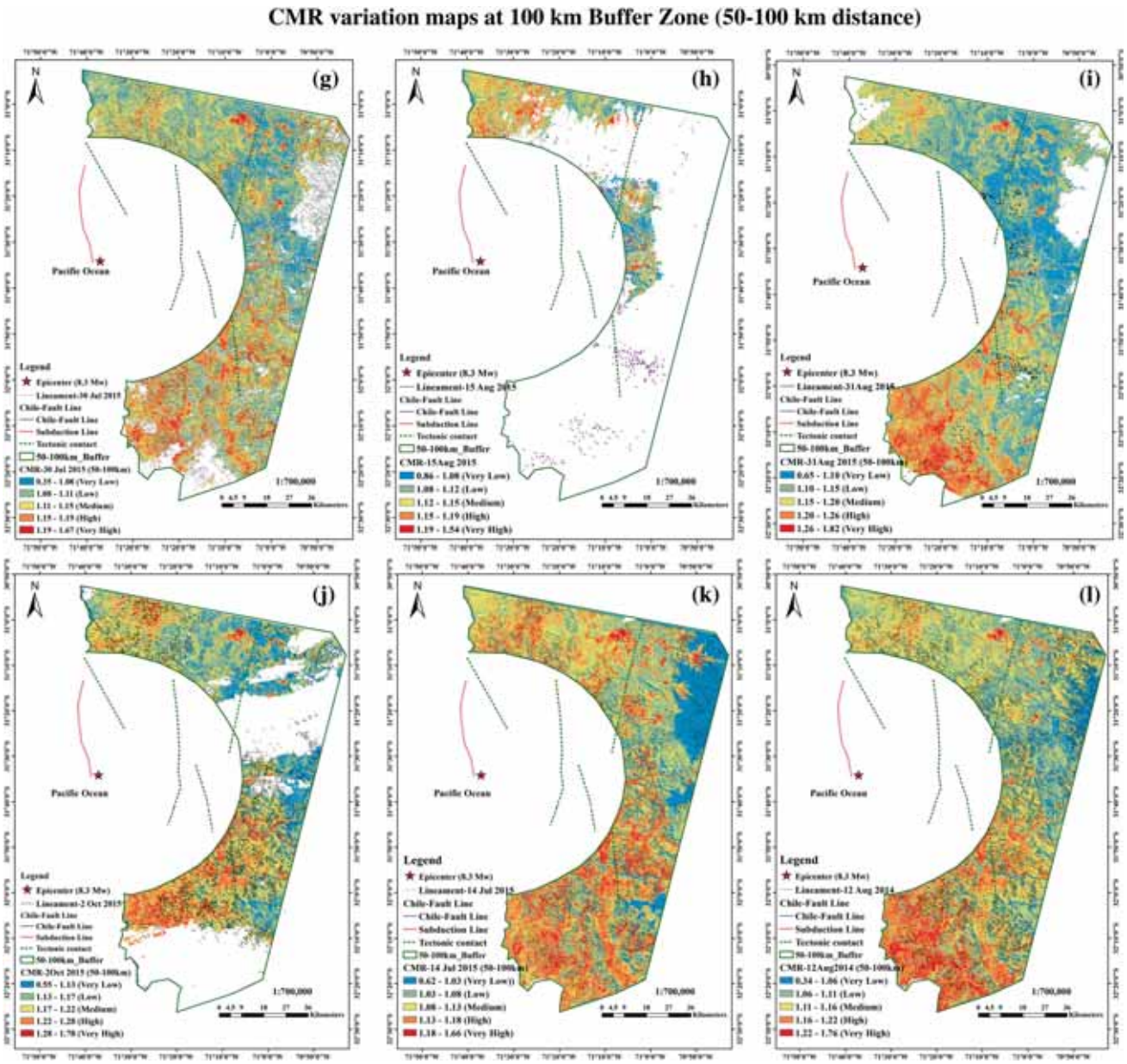

Figure 5. (*Continued.*)

and validated with two NEQ data of 2015 and 2014, respectively. In the 50, 100 and 150 km buffer range, on 14 July 2015, mean CMR values were observed as 1.11, 1.10 and 1.12, respectively, which represent a quite normal natural condition (figure 5e, k and q). Whereas, on 12 August 2014, the mean CMR values in all three buffer zones were observed as 1.14, 1.12 and 1.19, respectively, representing a normal scenario (figure 5f, l and r). Moreover, the two temporal NEQ datasets were followed in the geological structural settings of MCi, Tr, T and APZ (see figure 1b). These data variations help us to know the spatial variations as well as their extent in the geological settings.

For a better and more precise interpretation of CMR variations, 16 arbitral profiles were drawn in three buffer zones under the three transect sections (see figure 1c for overview). Based on all temporal CMR data, the first transect line was drawn on high to very high CMR pixel values within the 0–50 km buffer distance (figure 1c). In this section, location is part of the Mincha region under the Tr geological structure (figure 3b) and in the temporal profiles, it was marked as the alunite (Al–OH) signature (figure 6a–d). The

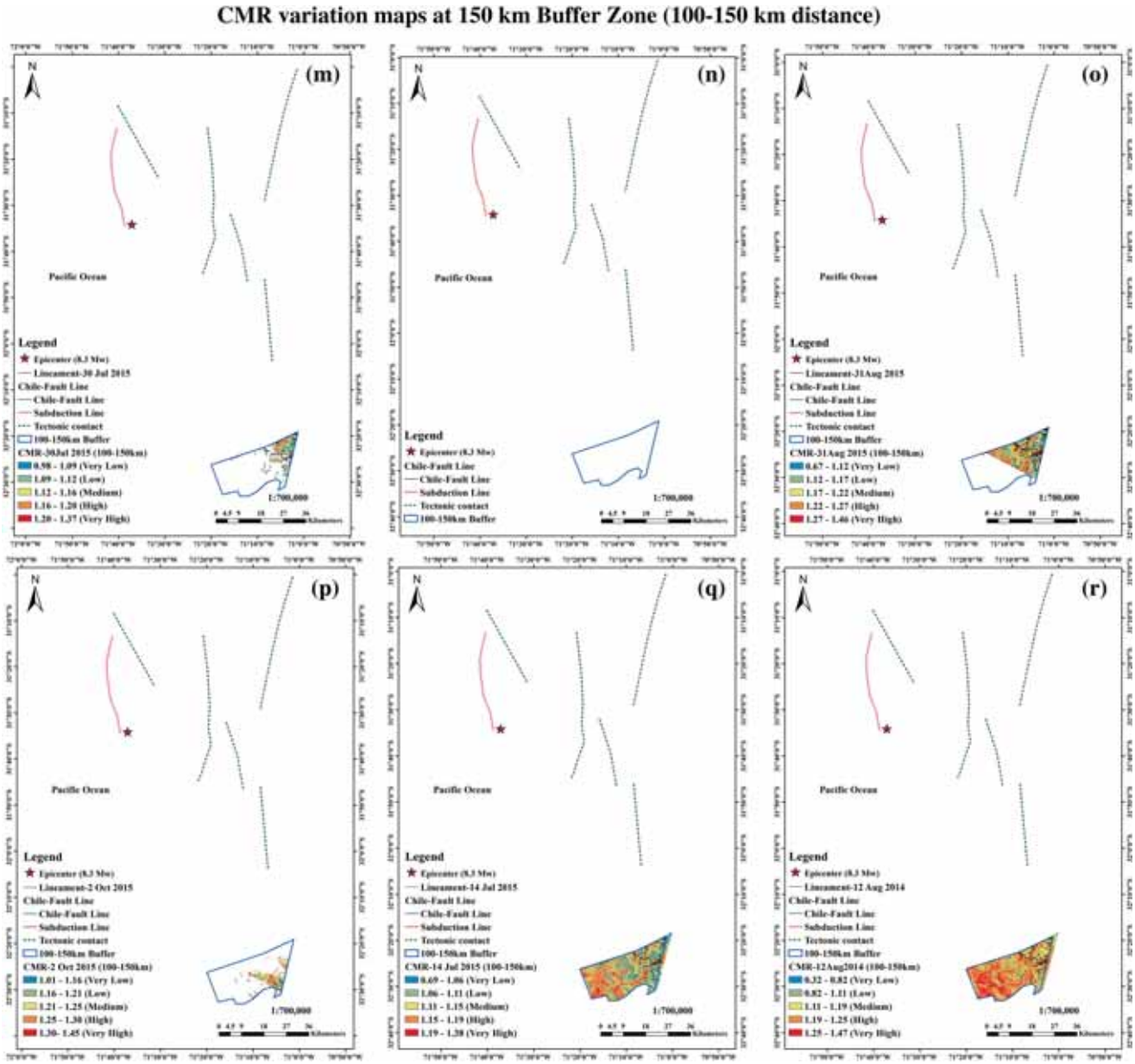

Figure 5. (*Continued.*)

second arbitral transect section drawing on very low to low CMR pixel values (highlighted in light blue to olive colour) within a 50–100 km buffer distance which is part of the Mincha region (northern part of image) under the K geological structure (figures 1c, 3c and 6k–p) indicate non-clay minerals and carbonate (CO_3) minerals in particular in this study, where the structural discontinuity or fault concentrations is quite low as verified through the extracted lineaments and fault data. Thereafter, the third arbitral transect section draws on medium CMR pixel values within the 100–150 km buffer distance. The location considered in this section is part of the Cabildo region in the southern part of the image falling under the MCi geological structure and in the transect profile, the black arrow head mark represents Kaolinite (figure 6g–j), which matched with the USGS spectral library profile (figures 1c and 3a). This kaolinite is the dominant clay mineral, with more than 50% of the total clay content present in this buffer zone. Two temporal transect profiles were not extracted from this zone due to the large-scale cloud presence as confirmed by the masked area represented with white pixels, thus excluded from figure 6.

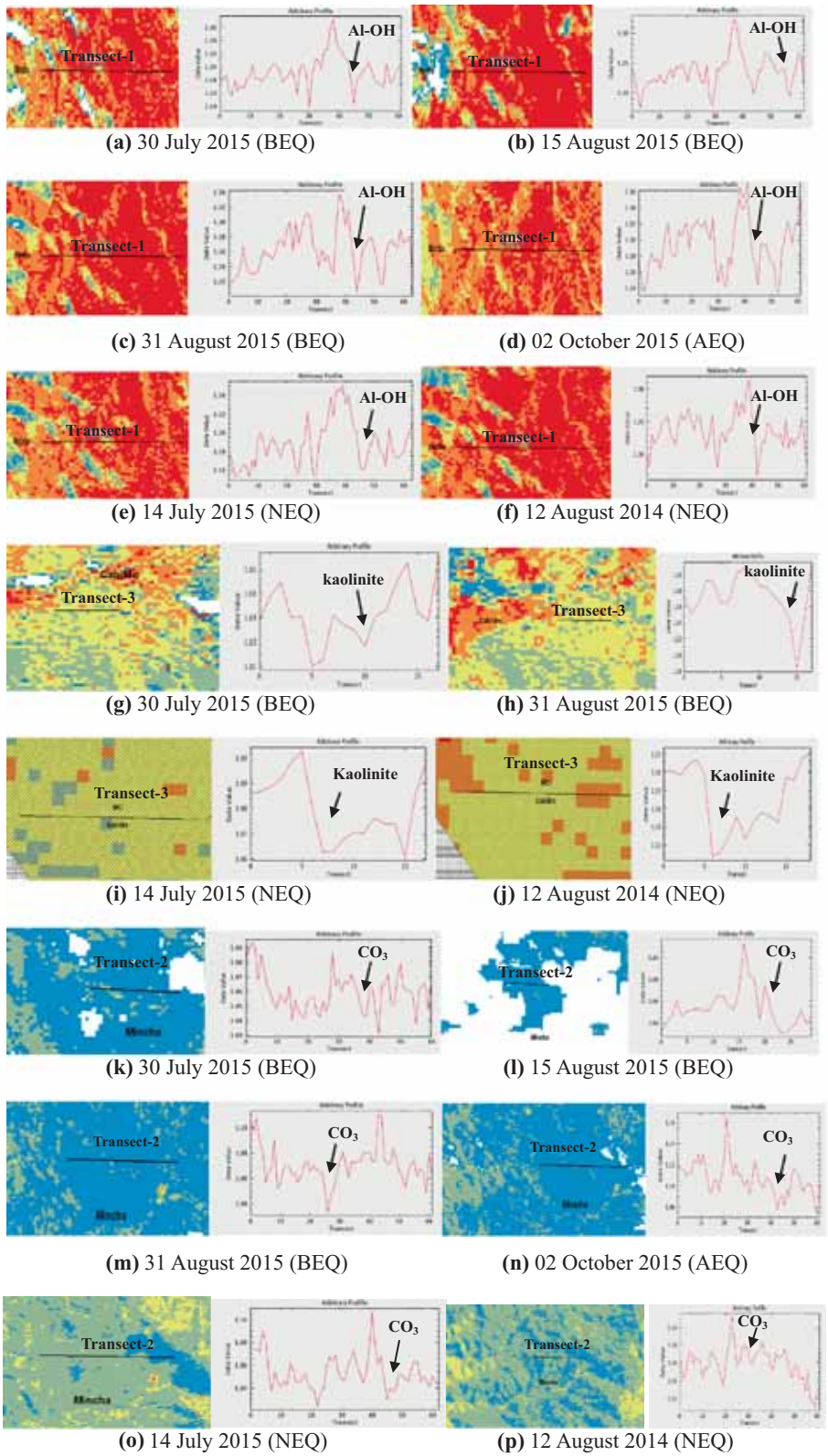

Figure 6. Three arbitral transect profile locations selected in three buffer zones for the CMR variations study at a spatio-temporal scale, where 16 arbitral transect profiles were extracted based on the CMR category pixel values. In the three buffer zones, transect overview is bounded with circles (see figure 1c) and in the present figure marked as Transect-1, Transect-2, and Transect-3, respectively, highlighted with the corresponding screenshots of CMR variations. (**a**–**f**) represents the alunite signature within the 0–50 km buffer zone on the Transect-1-line section, (**k**–**p**) represents carbonate minerals within the 50–100 km buffer zone on Transect-2 and (**g**–**j**) represents kaolinite dominant clay minerals within the 100–150 km buffer zone on Transect-3, respectively.

This high to very high CMR ratio pixel values help with the identification of the Al–OH minerals in the profile curve matched with the USGS spectral library curve (figure 6a–f). In this area, the presence of high lineament structural concentrations is pronounced in the 50 km buffer zone compared with the other two buffer zones which was confirmed through BEQ and AEQ lineaments data, represented by the masked CMR maps (figure 5a and d). In the transect-1 line, the value of the temporal CMR pixels observed was 1.27 on 30 July 2015, which gradually increased from 1.32 to 1.33 in the 15–31 August 2015 time period. The value of CMR pixels on 2 October 2015 was further increased and reached the maximum at 1.36. It is evident from these data that clay mineral variations existed in the study area and an alteration of minerals was first noticed on 15 August 2015 (i.e., 32 days BEQ), then it continued to increase in 2 October 2015 (i.e., 16 days AEQ). In transect-2, the CMR ratio was altered with the low pixel values ranging from 1.11 to 1.16 from 15 August 2015 to 2 October 2015, a sharp increase of 0.05 represents non-clay mineral concentrations. In transect-3 (50–100 km buffer), the CMR alteration was comparatively low BEQ (1.16–1.21) than in the 0–50 km buffer zone, showing a sharp increase of 0.05 until 31 August 2015. However, due to the presence of clouds BEQ (15 August 2015) and AEQ (2 October 2015), the CMR pixel values were not observed in the same transect line. In comparison with BEQ and AEQ data with NEQ, the CMR pixel values were found to be quite normal in the NEQ stage as observed for all three buffer zones (see figure 6, NEQ).

It should be noted that hydrothermally altered rocks associated with clay minerals (i.e., clay and alunite in this study) are highly pronounced and are located in MCi-igneous and metamorphic rocks, Tr and T-sedimentary rocks background. The northern and south-eastern parts of the image (figure 4c and d) are associated with low CMR pixel values with CO_3 mineral concentrations.

Moreover, based on the CMR pixel variations at three buffer zones during this short-time period (30 July 2015–2 October 2015), uncertainties and the uncertainties of the mean were quantified with the formula of equations (3) and (4) shown in section 3.2. Uncertainties of 0.05, 0.04 and 0.05 were observed and the uncertainties of the mean values are of $1.15 \pm 0.05, 1.31 \pm 0.04$ and 1.12 ± 0.05 estimated in the 0–50, 50–100 and 100–150 km buffer zones, respectively.

4.3 *Statistical analysis*

In the final stage of this study, variations were observed based on the derived and calculated statistical data, which are indicated in the following two paragraphs. First, based on the individual buffer zone, mean CMRs were simultaneously plotted for comparison and represented through a bar diagram with an error bar along with its trend line (figure 7a). In this case, in the 0–50 km buffer zone, the mean CMR value was increased BEQ from 15 to 31 August 2015 (figure 7a). Meanwhile, AEQ strike, mean CMR values still showed an increasing trend as observed on 2 October 2015, while it was quite normal in two values obtained from the NEQ time. Overall, in the 50–100 km buffer zone, the mean CMR values were quite lower compared to the 0–50 and 100–150 km buffer zones. However, if we considered a single time period on account of the 100–150 km buffer (e.g., 31 August 2015), mean CMR = 1.19 or 2 October 2015 (mean CMR = 1.23) BEQ and AEQ, it was always high in this buffer zone. Generally, the intensity of the earthquake decreased with distance away from the epicentre, and therefore, the mean CMR values should have less in the order of $150 < 100 < 50$ km for a single time period, but in this study, it differs to a certain extent. The high CMR values in the 100–150 km buffer is due to the possible presence of a clay or carbonate-rich structural arrangement as evident from the CMR pixel values, arbitral profile sections, the presence of regional complex geological structures (i.e., for clay minerals-Q, T, J from sedimentary rocks, and MCi-igneous and metamorphic rocks dominant, and for the carbonate-rich minerals geological unit K in the background in this buffer zone).

Meanwhile, the derived CMR pixel values suggest less error exist in the CMR index can be visualised through the error bar displayed (see figure 7a) and these errors have less impact on the CMR variations observed in this great magnitude earthquake study. The above discussion shows that BEQ, the study area observed subtle variations of mean CMR values in three different buffer zones, further continuing to increase even after the earthquake is over and which may have varied due to the equal influence of numerous environmental variables (i.e., weather, topography, solar radiation, geomorphology, geotectonic and the present tectonic stress field). The data variations clearly observed the STV of CMR exist BEQ and AEQ time. Based on this supportive evidence and CMR

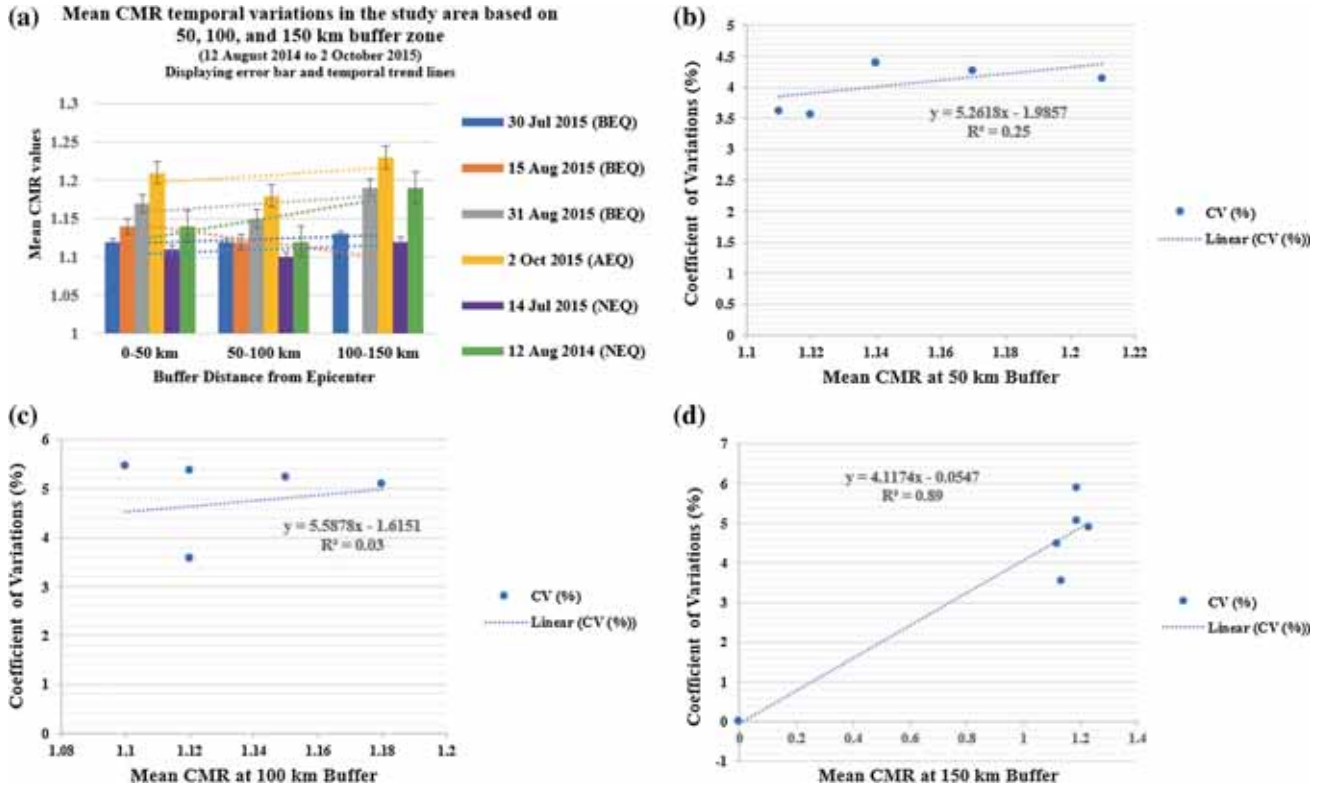

Figure 7. Mean CMR variations and error bars with trends observed in the study area and relationship between the mean CMR with the coefficient of variations (CV%): (**a**) bar diagram with error along with a trend line of mean CMR variations based on 50, 100 and 150 km buffer zone in consideration with the observed time under three different scenarios (i.e., BEQ, AEQ and NEQ); for the scatter diagram, each data point represents temporal mean values of the corresponding parameter at three different buffer zones; (**b**) mean CMR value at the 50 km buffer compared with CV; (**c**) mean CMR value at the 100 km buffer compared with CV; and (**d**) mean CMR value at the 150 km buffer compared with CV observed for the study regions, respectively.

values in all three buffer zones, six-trend lines were displayed along with a bar diagram, suggesting that mean CMR variations were higher in the 100–150 km distance than the other two counterparts and variations observed in the order of 150>100<50 km.

Secondly, the individual buffer-based mean CMR values were compared with the coefficient of variations (CV%) data to know the spatial variations and their relationship. In the 0–50 km buffer, mean CMR in values suggest a decreasing trend of CV% from 15 August 2015 (i.e., 32 days BEQ) to 2 October 2015 (i.e., 16 days AEQ) with an increasing tendency of mean CMR in BEQ. The similar phenomenon observed in AEQ, while the CV% and mean CMR showed a decreasing trend in NEQ time. In this study, the temporal datasets of mean CMR values were used to find out the trend of CV%. In the 0–50 km buffer scenario, it indicates a positive trend with a low coefficient of determination values (i.e., $R^2 = 0.25$) (figure 7b), in the 50–100 km buffer scenario, it also shows a positive trend with a very low value ($R^2 = 0.03$) (figure 7c). On the other hand, in the 100–150 km buffer scenario, a positive upward trend line was observed ($R^2 = 0.89$) for the CV%, the mean CMR values increased at this zone while CV% gradually decreased (figure 7d). Overall, the mean CMR data trend suggest that the variation (CV%) of CMR has subtly decreased in the 0–50 km buffer zone from 15 August 2015 (i.e., 32 days BEQ) to 2 October 2015 (i.e., 16 days AEQ). Similarly, variations (CV%) of CMR had increased from 15 August 2015 to 31 August 2015 and then subtly decreased on 2 October 2015 (i.e., 16 days AEQ) within the 50–100 and 100–150 km buffer zone.

5. Conclusion

The present study was conducted with the Landsat 8 OLI satellite sensor where the two band ratio approach of multispectral bands was used to obtain

the CMR images. Multi-temporal datasets of BEQ (three images), AEQ (one image) and NEQ (two images) were considered to observe the STV of CMR changes of the Illapel region during the Chile earthquake that struck on 16 September 2015. Furthermore, the data variations between the BEQ and AEQ periods were compared with two images of the NEQ period, along with structural information like temporal lineaments, regional geology and fault lines were used as supportive datasets for validation in the absence of field observation data and verified the output results derived from the image processing of the band ratio approach using the Landsat 8 OLI data. In this study, the CMR clearly highlights the spatio-temporal variations in the BEQ and AEQ time periods.

Moreover, the SWIR bands have a great advantage in extracting alteration information from remote sensing data. The band ratio of the SWIR 1: band 6 and SWIR 2: band 7 of Landsat 8 OLI was successfully used to estimate the CMR and prepare maps of the Illapel region based on the multi-temporal images which were further used for the buffer-based analysis. In the BEQ stage, Landsat 8 OLI sensor images were affected by clouds which acted as a problem for data extraction to a certain extent in the study area. This problem was resolved and masked out through the Fmask algorithm of MATLAB software, where clear land pixels were only considered for data extraction in the BEQ and AEQ evaluation. The two NEQ images were found to have less than 1% of the clouds coverage, thus it did not require further cloud masking operations and those radiance corrected images were used for data extraction. The data obtained by the Landsat 8 OLI sensor had a 30-m spatial resolution and contain the SWIR bands, thus this sensor is found to be well suited for CMR variations study. This study finally reached the following conclusions:

(i) The study proves the use of Landsat 8 OLI and can extract data well for the large areas using Landsat 8 OLI datasets.
(ii) The variations of CMR are pronounced in the 150 km buffer zone than in the other two buffer zones (i.e., 50 and 100 km buffer). The mean CMR was highly increased in 16 days BEQ in the Illapel region, which indicates the highest variations within the 150-km buffer zone and followed an increasing trend in the order of the $150 > 100 < 50$ km buffer.
(iii) The mean CMR values based on multi-temporal datasets of the great intensity earthquakes were successfully evaluated for this study which was highly sensitive in nature. The mean CMR increased by 0.02 and 0.05 on 32 and 16 days BEQ strike, which further increased by 0.04 AEQ. These data variations of the mean CMR varied along the regional geological fault lines in the BEQ and AEQ time periods, whereas the above mentioned time period values were found to be normal while we compared with two temporal datasets of the NEQ time.
(iv) The highly observed data variations of this parameter within a 150 km buffer zone are ideally complex for the target area of the epicentre as the distance keeps getting longer. However, Landsat 8 OLI sensor is suitable to observe the spatio-temporal variations in the BEQ and AEQ time periods as considered in this study.
(v) A band ratio of band 6-SWIR 1 (1.57–1.65 μm) and band 7-SWIR 2 (2.11–2.29 μm) is found useful for CMR determination, which thus helps with the observation and is used for temporal changes investigation of the CMR.
(vi) The CMR pixel values were further confirmed using the temporal datasets with the 16 arbitral transect profiles constructed in the selected three transect lines in the three buffer zones, clearly defining the CMR variations with patterns of signatures (i.e., clay, alunite, carbonate minerals) verified with the regional geology, lineaments and fault lines in the background to some extent.

It can be concluded from this study that our methodology might be useful as an alternative approach for the frequent monitoring and investigation of CMR changes in this area throughout the year. This study was conducted in the absence of field observation data which is its only shortcoming. To minimise this shortcoming, regional structural data have been derived from the same data source using Landsat 8 OLI. However, this study also recommends that it can be further compared with studies on other medium, strong and great magnitude earthquakes in the same or different regions of the world along with field data for future earthquake investigations.

Acknowledgements

This work was supported by the Major State Basic Research Development Program of China

(973 Program) (No. 2013CB733405) and the National High Technology Research and Development Program of China (863 Program) (No. 2014AA06A511) and Chinese Academy of Sciences and The World Academy of Sciences (CAS-TWAS) President's Fellowship-2015 (No. 2015CTF024) awarded by the University of the Chinese Academy of Sciences (UCAS) and we offer our sincere thanks to the USGS earth explorer committee for providing the Landsat 8 OLI Imageries from their archive for free. The authors would like to offer their special and sincere thanks to the editor, associate editor, and the two anonymous reviewers for their valuable and insightful comments and suggestions received during the review stages, which were greatly helpful in improving the quality of this paper.

References

Al Rawashdeh S, Bassam S and Hamzah M 2006 The use of remote sensing technology in geological investigation and mineral detection in El Azraq-Jordan; *Cybergeo: Eur. J. Geog. Syst. Model. Geostats.* **2856** 203–219.

Barton C A, Zoback M D and Moos D 1995 Fluid flow along potentially active faults in crystalline rock; *Geology* **23** 683–686.

Caine J S, Evans J P and Forster C B 1996 Fault zone architecture and permeability structure; *Geology* **24** 1025–1028.

Chen J P, Wang Q J, Dong Q J and Cong Y 2009a Extraction of remote sensing alteration information in tuotuohe, qinghai province; *Earth Sci.-J. China Univ. Geosci.* **2** 314–318 (in Chinese with English Abstract).

Chen J M, Sun W D and Yan B K 2009b The application and research of the anomaly extraction process based on the ASTER multi-spectral remote sensing in Tianhu iron ore mine, Xinjiang; *Geology* **27** 368–372 (in Chinese with English Abstract).

Chester F M, Evans J P and Biegel R L 1993 Internal structure and weakening mechanisms of the San Andreas fault; *J. Geophys. Res.* **98** 771–786.

Chester F M and Logan J M 1986 Composite planar fabric of gouge from the Punchbowl fault, California; *J. Struct. Geol.* **9** 621–634.

CNN 2015 Chile Earthquake: 11 killed, aftershocks continue-CNN-CNN.com, https://edition.cnn.com/2015/09/17/americas/chile-earthquake/index.html.

Drury S A 1987 *Image interpretation in geology* (2nd edn); Allen and Unwin, London, 243p.

Drury S A 1993 *A review of image interpretation in geology* (2nd edn); Chapman and Hall, London, 283p.

Fitts T G and Brown K M 1999 Stress-induced smectite dehydration ramifications for patterns of freshening fluid expulsion in the N. Barbados accretionary wedge; *Earth Planet. Sci. Lett.* **172** 79–197.

Forster C B, Goddard J V and Evans J P 1991 Hydrology of thrust faults and crystalline thrust sheets: Results of combined field and modeling studies; *Geophys. Res. Lett.* **18** 979–982.

Gad S and Kusky T 2007 ASTER spectral ratioing for lithological mapping in the Arabian–Nubian Shield, the Neoproterozoic Wadi Kid area, Sinai, Egypt; *Gondwana Res.* **11** 326–335.

Geologic Map-Catalog Data Gov 2018 DATA.GOV, DATA CATALOG, https://catalog.data.gov/dataset?tags=geologic+map, South America Geologic Map (geo6ag), https://catalog.data.gov/dataset/south-america-geologic-map-geo6ag.

Geology Indices Background, Harris Geospatial Solutions, Documentation Center, Clay Minerals Ratio; https://www.harrisgeospatial.com/docs/backgroundgeologyindices.html#clay.

Geotech-Geotechcenter.org 2018 Map Library and Data Resources, Data-General Interest-World Wide data – http://www.gadm.org/country, Download GADM Data (version 3.6), Country: Chile-Shapefile, gadm_36_CHL_shp.zip; https://gadm.org/download_country_v3.html.

GitHub-cossatot/gem-global-active-faults, GEMScienceTools/gem-global-active-faults/zip/master; https://github.com/cossatot/gem-global-active-faults.git.

Gupta R P, Saraf A K and Chander R 1998 Discrimination of areas susceptible to earthquake induced liquefaction from landsat data; *Int. J. Remote Sens.* **19** 569–572.

Hickman S 1991 Stress in the lithosphere and the strength of active faults; In: *U. S. National report international union geodesy and geophysics 1987–1990*, *Contributions in tectonophysics* (ed.) Shea M A, American Geophysical Union, Washington DC, pp. 759–775.

Hoppin R A, Manley R D, Tappmeyer D M and Voldseth N E 1973 Geologic interpretations of ERTS-1 imagery, bighorn mountains; *Contr. Geol.* **12**(**2**) 32–42.

Houston R S 1973 Geologic mapping using space images; *Rocky Mount. Geol.* **12**(**2**) 77–97.

Hung L Q, Batelaan O and De S F 2005 Lineament extraction and analysis, comparison of Landsat ETM and ASTER imagery. Case study: Suoimuoi tropical karst catchment, Vietnam; *Proc. SPIE* **5983** 1–12.

Inzana J, Kusky T, Higgs G and Tucker R 2003 Supervised classifications of landsat TM band ratio images and landsat TM band ratio image with radar for geological interpretations of central Madagascar; *J. Afr. Earth Sci.* **37** 59–72.

Jensen M L and Bateman A M 1981*Economic mineral deposits*; Wiley, USA, 593p.

Khan S D and Mahmood K 2008 The application of remote sensing techniques to the study of ophiolites; *Earth-Sci. Rev.* **89** 135–143.

Kuo L W, Song S R, Yeh E C, Chen H F and Si J 2012 Clay mineralogy and geochemistry investigations in the host rocks of the chelungpu fault, Taiwan: Implication for faulting mechanism; *J. Asian Earth Sci.* **59** 208–218.

Lillesand T, Kiefer R W and Chipman J 2015 *Remote sensing and image interpretation* (7th edn); Wiley, USA, 736p.

Madani A, Rahman A E M, Fawzy K M and Emam A 2003 Mapping of the hydrothermal alteration zones at haimur gold mine area, south eastern desert, Egypt using remote

sensing techniques; *Egypt. J. Remote Sens. Space Sci.* **6** 47–60.

Massironi M, Bertoldi L, Calafa P, Visona D, Bistacchi A, Giardino C and Schiavo A 2008 Interpretation and processing of ASTER data for geological mapping and granitoids detection in the sagho massif (easter Anti-Atlas, Morocco); *Geosphere* **4**(**4**) 736–759.

Mohanty K K, Maiti K and Nayak S 2001 Monitoring water surges; *GIS Develop.* **3** 32–33.

Moore J C 1989 Tectonics and hydrogeology of accretionary prisms: Role of the decollement zone; *J. Struct. Geol.* **11** 95–106.

Mwaniki M W, Moeller M S and Schellmann G 2015 A comparison of Landsat 8 (OLI) and Landsat 7 (ETM+) in mapping geology and visualizing lineaments: A case study of central region Kenya; In: *ISPRS – international archives of the photogrammetry, remote sensing and spatial information sciences*, Vol. **XL-7(W3)**, pp. 897–903; *36th international symposium on remote sensing of environment*, 11–15 May 2015, Berlin, Germany.

Newman J and Mitra G 1994 Fluid-induced deformation and recrystallization of dolomite at low temperature along a natural fault zone, mountain city window, Tennessee; *Geol. Soc. Am. Bull.* **106** 1267–1280.

Pour B A and Hashim M 2015 Hydrothermal alteration mapping from landsat 8 data, Sar cheshmeh copper mining district, South-eastern Islamic Republic of Iran; *J. Taibah Univ. Sci.* **9**(**2**) 181–196.

Pour B A, Hashim M and van Genderen J 2013 Detection of hydrothermal alteration zones in a tropical region using satellite remote sensing data: Bau gold field, Sarawak, Malaysia; *Ore Geol. Rev.* **54** 181–196.

Ray C D K, Foreste K and Roy P S 2001 Detection and analysis of surface changes due to recent earthquake in Gujarat using IRS PAN and LISS-III data; In: *Proceedings of the workshop on recent earthquake of Chamoli and Bhuj*, 22–23 May 2001, Indian Society of Earthquake Technology, Roorkee, India, pp. 225–236.

Sabins F F Jr 1987 *Remote sensing: Principles and interpretation* (2nd edn); Freeman, San Francisco: New York, 499p.

Sabins F F 1999 Remote sensing for mineral exploration; *Ore Geol. Rev.* **14** 157–183.

Saraf A K 2000 IRS IC-PAN depicts Chamoli earthquake induced landslide in Garhwal Himalayas, India; *Int. J. Remote Sens.* **21** 2345–2352.

Sharma J R, Gupta A K, Sreenivasan G and Bhadra B K 2003 Damage Assessment of Bhuj earthquake (2001) using IRS LISS-III and PAN data; In: *Proceedings of the international workshop on earth system process related to Gujarat earthquake using space technology*, 27–29 January 2003, Department of Civil Engineering, IIT Kanpur, India.

Si J, Li H, Kuo L, Pei J, Song S and Wang H 2013 Clay mineral anomalies in the Yingxiu–Beichuan fault zone from the WFSD-1 drilling core and its implication for the faulting mechanism during the 2008 Wenchuan earthquake (Mw 7.9); *Tectonophys.* **619–620** 171–178.

Singh R P, Bhoi S, Sahoo A K, Raj U and Ravindranath S 2001 Surface manifestations after the Gujarat Earthquake; *Curr. Sci.* **81**(**2**) 164–166.

Solaro G, Novellis V D, Castaldo R, Luca C D, Lanari R, Manunta M and Casu F 2016 Co seismic fault model of Mw 8.3 2015 Illapel earthquake (Chile) retrieved from multi orbit sentinel 1-A DInSAR measurements; *Remote Sens.* **8**(**323**) 1–14.

Towhata I 2008 Stress–Strain models; In: *Geotechnical earthquake engineering, Springer Series in geomechanics and geoengineering* (1st edn); (ed.) We Wei, Springer-Verlag, Berlin, Heidelberg, pp. 217–234.

USGS 2015 Earth explorer-Landsat 8 OLI archive, http://earthexplorer.usgs.gov.

USGS 2015 M 8.3–48 km W of Illapel, Chile; Earthquake Hazards Program, https://earthquake.usgs.gov/earthquakes/eventpage/us20003k7a/executive.

Vrolijk P and van der Pluijm B A 1999 Clay gouge; *J. Struct. Geol.* **21** 1039–1048.

Warr L N and Cox S 2001 Clay mineral transformations and weakening mechanisms along the alpine fault, New Zealand; In: *The nature and tectonic significance of fault zone weakening* (eds) Holdsworth R E, Strachan R A, Magloughlin J F and Knipe R J, Vol. **186**; Special Publications, Geological Society, London, pp. 85–101.

Warr L N, Greiling R O and Zacrisson E 1996 Thrust-related very low-grade metamorphism in the marginal part of an orogenic wedge, Scandinavian Caledonides; *Tectonics* **15** 1213–1229.

Wintsch R P, Christoffersen R and Kronenberg A K 1995 Fluid-rock reaction weakening of fault zones; *J. Geophys. Res.* **100**(**B7**) 13021–13032.

Zhang T, Yi G, Li H, Wang Z, Tang J, Zhong K, Li Y, Wang Q and Bie X 2016 Integrating data of ASTER and landsat 8-OLI (AO) for hydrothermal alteration mineral mapping in duolong porphyry Cu-Au deposit, Tibetan plateau, China; *Remote Sens.* **8**(**890**) 1–23.

Zoback M D, Zoback M L, Mount V S, Suppe J, Eaton J P, Healy J H, Oppenheimer D, Reasenberg P, Jones L, Raleigh C B, Wong I G, Scotti O and Wentworth C 1987 New evidence on the state of stress on the San Andreas fault system; *Science* **238**(**4830**) 1105–1111.

Corresponding editor: Arkoprovo Biswas